

# Image-based crystal plasticity FE framework for microstructure dependent properties of Ti–6Al–4V alloys

J. Thomas<sup>a</sup>, M. Groeber<sup>b</sup>, S. Ghosh<sup>c,\*</sup>

<sup>a</sup> Mechanical Engineering, The Ohio State University, Columbus, OH 43210, USA

<sup>b</sup> AFRL/RXLM, Bldg 655, Rm 079, 2230 Tenth Street, Wright-Patterson AFB, OH 45433, USA

<sup>c</sup> Civil Engineering and Mechanical Engineering, Johns Hopkins University, Baltimore, MD 21218, USA

## ARTICLE INFO

### Article history:

Received 1 February 2012

Received in revised form 30 May 2012

Accepted 2 June 2012

Available online 9 June 2012

### Keywords:

Crystal plasticity FEM

Virtual microstructure

Creep

Sensitivity

Microstructure-response

Titanium alloys

Polycrystalline

## ABSTRACT

In this paper, micromechanical crystal plasticity finite element method (CPFEM) simulations of the response of virtual/synthetic  $\alpha$ - $\beta$  Ti–6V–4Al polycrystalline microstructures are carried out to quantify the effect of the material's microstructure on mechanical properties. The image-based CPFEM analysis begins with characterization of the morphological and crystallographic features of the material at the scale of the polycrystalline microstructure. Statistically equivalent representative 3D polycrystalline microstructures are generated from the microstructural characterization data and subsequently discretized into finite element meshes for the CPFEM analysis. Using a validated computational analysis tool, sensitivity studies are performed to develop a quantitative understanding of how individual microstructural parameters affect the overall mechanical response properties of the alloy. Functional forms of the dependencies are proposed that connect the material's microstructural features to properties like yield strength response, constant strain rate response and creep response.

© 2012 Elsevier B.V. All rights reserved.

## 1. Introduction

Titanium alloys are widely used in a number of applications ranging from aerospace, medical to sporting goods industries [1]. Titanium alloys exhibit a cold creep phenomena, where time-dependent deformation is seen to occur at room temperature and at loads as low as 60% of yield strength [2–9]. The cold creep mechanism, being at low homologous temperatures, is not diffusion-mediated, but occurs due to dislocation glide where dislocations are arrayed in a planar fashion [6]. It is strongly dependent on crystallographic orientation in titanium [2,10]. It is well known that microstructural features directly affect mechanical properties, e.g. creep, of polycrystalline materials. In [11–13], functional relations on microstructure dependencies have been created through use of neural network fuzzy logic modeling of large datasets that are created from experiments conducted on microstructures generated through different heat treatments and thermomechanical processing. There is a large cost associated with the processing and testing of real samples. A second downside of this experimental approach is that it is very difficult to vary one microstructural feature while holding the others constant during heat treatment

processing because the evolution of most of these important features is highly coupled.

Image-based modeling and simulations, using crystal-plasticity finite element method or CPFEM analyses of polycrystalline microstructures, is an attractive alternative to the experimental methods for determining microstructure–property relationships. These models capture details of microstructural features, including crystallographic orientations, misorientations, grain morphology and their distributions for good predictive capability. Ghosh et al. [14–16] have developed time-dependent, image-based crystal plasticity models, accounting for large strains, material anisotropy, tension–compression asymmetry and size dependence, for analyzing the mechanical response of titanium alloys. The models are able to represent the complex microstructures of Ti–64 and Ti–6242 alloys consisting of transformed  $\beta$  colonies with alternating  $\alpha$  (hcp) and  $\beta$  (bcc) lamellae in a matrix of equiaxed primary  $\alpha$  (hcp) grains. Image-based computational models in [17,18] account for morphology and orientation distributions from orientation imaging microscopy (OIM) images of the microstructure. Numerical simulations of 3D Ti–6242 microstructures are conducted to understand creep-induced load shedding behavior. A grain level fatigue crack nucleation criterion, based on the theory of crack evolution at the tip of a dislocation pileup, is also developed for cold dwell in Ti–6242 alloys in [19,20]. One of the beneficial aspects of image-based CPFEM modeling is that a large number of virtual specimens with different microstructural features can be generated and tested at

\* Corresponding author. Tel.: +1 410 516 7833; fax: +1 410 516 7473.  
E-mail address: [sghosh20@jhu.edu](mailto:sghosh20@jhu.edu) (S. Ghosh).

a low cost compared with testing of real specimens. In contrast to the limitations of experimentally generating microstructural variations, it is easy to vary the microstructural features of these virtual specimens independently to gain a more direct understanding of their effect on properties. It is important that the models be experimentally validated and efficient for simulating a large number of grains in the polycrystalline aggregate.

The present paper is aimed at developing a quantitative understanding of the role of microstructure on the rate-dependent plastic response of the titanium alloy Ti–6Al–4V using a comprehensive CPFEM analysis based approach. The overall process encompasses 2D microstructural characterization, 3D microstructure model creation, mesh generation and subsequently, CPFEM analysis and data processing. Quantitative characterization of material microstructures is accomplished through SEM image analysis, EBSD data collection, stereological procedures and statistical quantification. Subsequent to material characterization and data acquisition, a 3D reconstruction code developed in [21] is used to create statistically equivalent, virtual microstructures that are meshed for computational simulations. Crystal plasticity FEM simulations and analyses are conducted for strain-rate controlled and creep tests and compared with experimental results for validating the model. Virtual microstructures with varying characteristic functions are generated and analyzed to gain an understanding of response sensitivities to the microstructure. Functional forms of plasticity and creep models are proposed which provide a direct quantitative connection between microstructural features and the constant strain rate and creep response of the material.

## 2. 3D virtual polycrystalline microstructure simulation and mesh generation

This section discusses 2D characterization of OIM surface images, and generation of 3D polycrystalline microstructure models and meshes from the 2D data. 3D microstructures have been generated by a variety of different techniques including Focused Ion Beam (FIB) based methods, sectioning methods [22–24], manual polishing based methods [25] and X-ray tomography methods [26]. These methods require 3D data for microstructure reconstruction. The present work employs a method of estimating 3D statistics from extrapolation of 2D surface measurements and data on polycrystalline specimens. The reconstruction algorithm is based on stereology [27], a method of creating statistically equivalent 3D morphologies from 2D measurements.

### 2.1. Microstructural characterization of the $\alpha$ – $\beta$ Ti–6Al–4V

Ti–6Al–4V alloy specimens are imaged using an FEI Sirion Scanning Electron Microscope. Three sets, consisting of seven images each, at magnifications of 750 $\times$ , 1000 $\times$ , and 1500 $\times$ , respectively are acquired. A typical image at 1000 $\times$  magnification is shown in Fig. 1. The microstructure of the  $\alpha$ – $\beta$  Ti–6Al–4V alloy consists of 2 major phases, viz. (i) transformed  $\beta$  colonies consisting of alternating  $\alpha$  (hcp) and  $\beta$  (bcc) lamellae and (ii) equiaxed primary  $\alpha$  grains (hcp). In the transformed  $\beta$  colonies,  $\alpha$  and  $\beta$  lamellae are experimentally observed to have volume fractions of approximately 88% and 12%, respectively [15]. The crystallographic orientations are influenced by the  $\beta$ -to- $\alpha$  phase transformation. The orientations of the  $\alpha$  and  $\beta$  lamellae follow a specific Burgers orientation relationship [3], expressed as  $(101)_{\beta} \parallel (0001)_{\alpha}$ ,  $[1\bar{1}\bar{1}]_{\beta} \parallel [2\bar{1}10]_{\alpha}$ . This relation brings the hcp  $\mathbf{a}_1$  slip direction into coincidence with the bcc  $\mathbf{b}_1$  slip direction. The resulting material has a misorientation distribution with preferences to certain variants [28]. Fig. 4 shows the misorientation distribution (MoDF) of the specimen used in this work. This distribution is comparable to that seen for a similarly processed

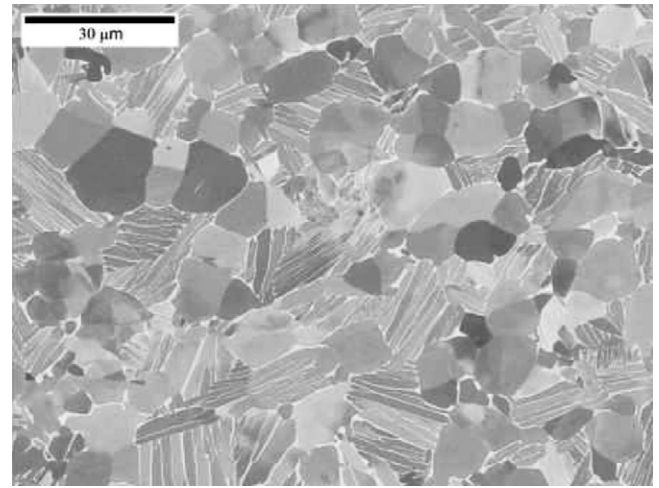


Fig. 1. A typical microstructural image of  $\alpha$ – $\beta$  Ti–6Al–4V alloy at 1000 $\times$  magnification.

Ti–6Al–4V in [28]. The images are analyzed using stereological techniques and assumptions described in [29]. Relevant morphological data representing important microstructural features that affect material response [13,30] are given in Table 1.

The average grain and colony size in the table are defined in terms of an equivalent sphere diameter or ESD. For determining the ESD, the equivalent projected circle diameters (ECD) are first computed using standard image analysis techniques. An assumption is subsequently made that the grains or colonies are spherical in 3D space. Using the principles of stereology, their size can be approximated by the following formula, which connects the  $\overline{ECD}$  to the ESD of a sample, i.e.

$$\overline{ESD} = \frac{4}{\pi} \overline{ECD}. \quad (1)$$

In [24] it has been observed that the log-normal probability density function provides a reasonable fit to the grain and colony size data of Ni microstructures. The log-normal probability density function, defined using two parameters viz. the average and standard deviation of the population, is also found to adequately represent the grain size distribution of the Ti–6Al–4V alloy samples. The good agreement with experimental data is shown in Fig. 2. Approximately 50 distributions are tested in this work using a maximum likelihood estimation approach [31]. Consequently, the log-normal distribution is found to be suitable for generation of statistically equivalent virtual or synthetic microstructures in this paper.

In addition to morphological analysis, crystallographic orientation data is obtained through electron back-scattered diffraction or EBSD scans of specimen surfaces containing approximately 1000 grains and colonies. The scans are obtained using an FEI Quanta SEM and processed using codes described in [21,24] to acquire data on orientation distribution of the hcp phase, as well as on misorientation and micro-texture distributions. These distributions are depicted in Figs. 3–5, respectively. While grain misorientation is assessed from the 2D EBSD surface scans along the length of grain

Table 1  
Morphological data determined from SEM images and stereology.

Parameter	Description	Value
$D$	Average grain/col. size	11.9 $\mu\text{m}$
$S^d$	Stand. dev. grain/col. size	5.22 $\mu\text{m}$
$l_{\alpha}$	$\alpha$ lath thickness	0.29 $\mu\text{m}$
$l_{\beta}$	$\beta$ rib thickness	0.089 $\mu\text{m}$
$V_f$	Vol. fract. of globular $\alpha$	49.9%
$V_{fr}$	Vol. fract. of total $\alpha$ phase	93%

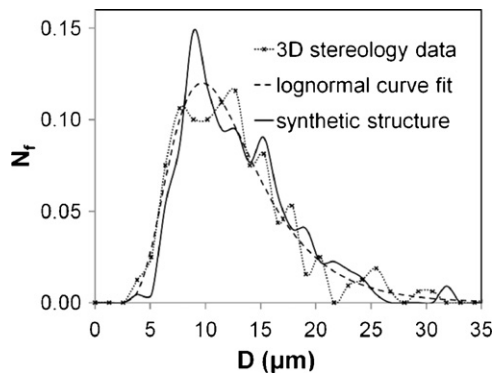


Fig. 2. Comparison of grain and colony size  $D$ , distribution.  $N_f$  is the number fraction of grains or colonies.

boundary, it is assumed to be equivalent across a grain boundary surface area in the 3D synthetic structure generation process. This is a reasonable assumption, given the fact that matching is done based on a non-dimensional fraction obtained by normalizing the data from either total grain boundary length (in 2D) or the total grain boundary surface area (in 3D). Orientations of the  $\beta$  lamellae are not directly obtained from the EBSD scan because of their small size. However, they are uniquely defined from the Burger's relationship using the orientation of the adjacent  $\alpha$  phase and the lamellar structure of the transformed  $\beta$  colonies. The orientation information for each of the  $\alpha$  and  $\beta$  phases is required in the crystal plasticity models for FEM simulations [15].

## 2.2. Virtual polycrystalline microstructure simulation procedure

The virtual or synthetic polycrystalline microstructure simulation is performed using methods and codes described in [21,24],

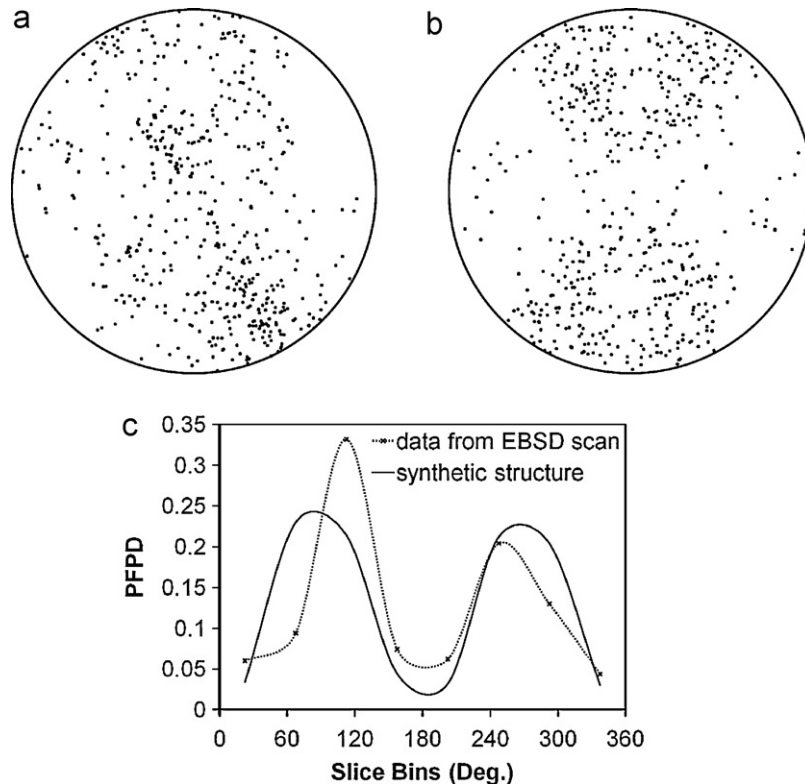


Fig. 3.  $\alpha$ -Phase (0002) pole figures for: (a) sample data and (b) synthetic structure, and (c) pole figure point density (PPFD) distributions of the 2 pole figures for a more quantitative comparison of the crystallography.

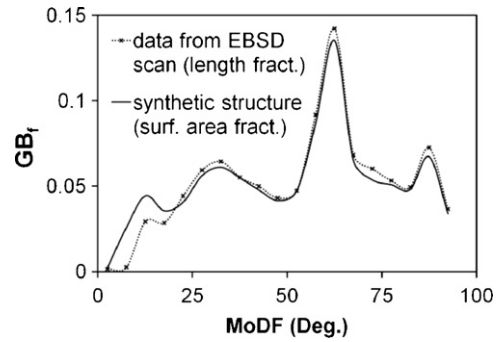


Fig. 4. Misorientation distribution (MoDF) comparison.  $GB_f$  corresponds to either grain/colony boundary length fraction or grain/colony boundary surface area fraction.

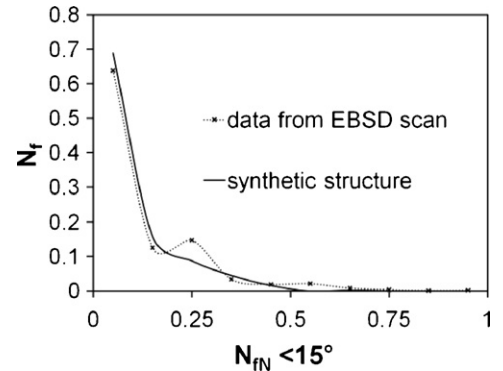


Fig. 5. Microtexture distribution comparison where microtexture is defined by the number fraction of neighbors ( $N_{fN}$ ) with misorientation less than  $15^\circ$ .  $N_f$  is the number fraction of grains/colonies.

where microstructures are generated by matching morphological and crystallographic statistics. While the grain and colony statistics are generated using a spherical assumption in the characterization phase, this assumption is relaxed when generating the virtual 3D microstructure. Grain shapes are allowed to deviate from the sphere when actually placed in the ensemble. The morphological orientations of these virtual grains are assumed to be random and they are placed in the aggregate based on neighborhood constraints. The average number of neighbors is assumed to be approximately 14 grains, with some variation according to grain size. This choice of 14 neighbors has been corroborated for the superalloy IN100 in [24], where it has been seen that the number of neighbors of a grain is strongly correlated to its size. This assumption of correlation between the number of neighbors of a grain to its size implies a lack of clustering of similarly sized grains, i.e. random neighborhoods, which appears to be valid when viewing the 2D micrographs. Once the voxelized morphological structure has been built, the grains and colonies with hcp lattice structure are assigned orientations based on a random sampling from the orientation distribution functions. Misorientation and micro-texturing statistics are matched by an iterative process, where orientations are allowed to switch between grains/colonies or be replaced by new random orientations, while error is tracked and compared to sample statistics until convergence is attained. Details of this process are given in [15,16].

The results of the microstructural simulation procedure are validated by comparing the sample statistics with the statistics of the virtual microstructure. Figs. 2–5 show graphical comparisons of the sample statistics with a 500-grain synthetically generated 3D microstructure. Generally good agreement allows the synthetic structure to be considered as statistically equivalent to the experimental microstructure.

One possible reason that the pole figure point density (PFPD) distributions in Fig. 3(c) do not match well is due to the 2D to 3D assumption. The sample EBSD scan is analyzed and the individual orientations are binned assuming surface area fraction of the grains, corresponding to a 2D measurement. In the synthetic structure, orientations are assigned to the grains based on the volume fraction of the grains, which is 3D measurement. It is noted that the MoDF and the TDF statistics do match closely. Thus, these higher order crystallographic statistics are seen not to be affected as much by the 2D to 3D assumption. In contrast to the ODF, both the MoDF and TDF depend on the grains' neighbors. It is quite possible that the grain neighborhood dependence tends to attenuate the effect of the 2D to 3D assumption in the MoDF and TDF.

The virtual microstructure generation code may be used to generate structures with any number of grains. Figs. 2–5 show statistics of a 500-grain structure. It is seen that for microstructures in excess of 300 grains, the validation algorithm converges to a small error defined by the root mean square errors of the mean and standard deviation of grain/colony size. The root mean square error for average grain/colony size is defined as:

$$E_{av} = \sqrt{\sum_i (A_i^{av} - \overline{ESD})^2} \quad (2)$$

where  $A_i^{av}$  is the average grain/colony size of the microstructures generated with  $i$  grains and the average equivalent sphere diameter  $\overline{ESD}$  in this case is 11.9  $\mu\text{m}$ . The root mean square error for the standard deviation of grain/colony size is defined as:

$$E_{sd} = \sqrt{\sum_i (A_i^{sd} - S^{sd})^2} \quad (3)$$

where  $A_i^{sd}$  is the standard deviation of grain/colony size of structures generated with  $i$  grains and  $S^{sd}$  is the standard deviation

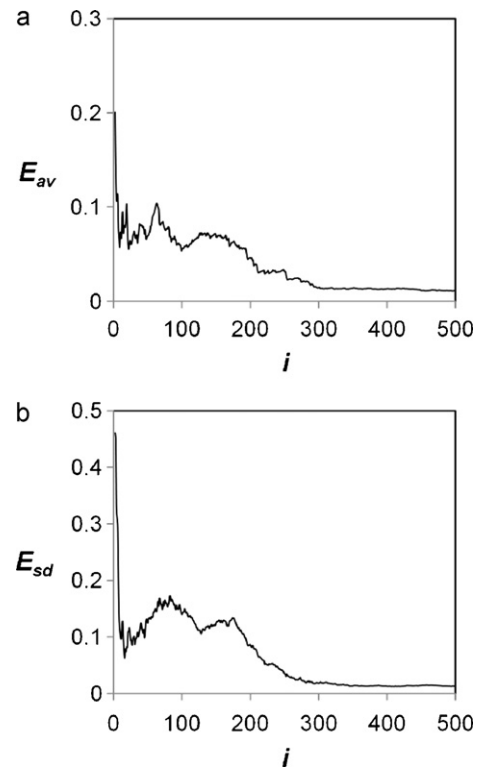
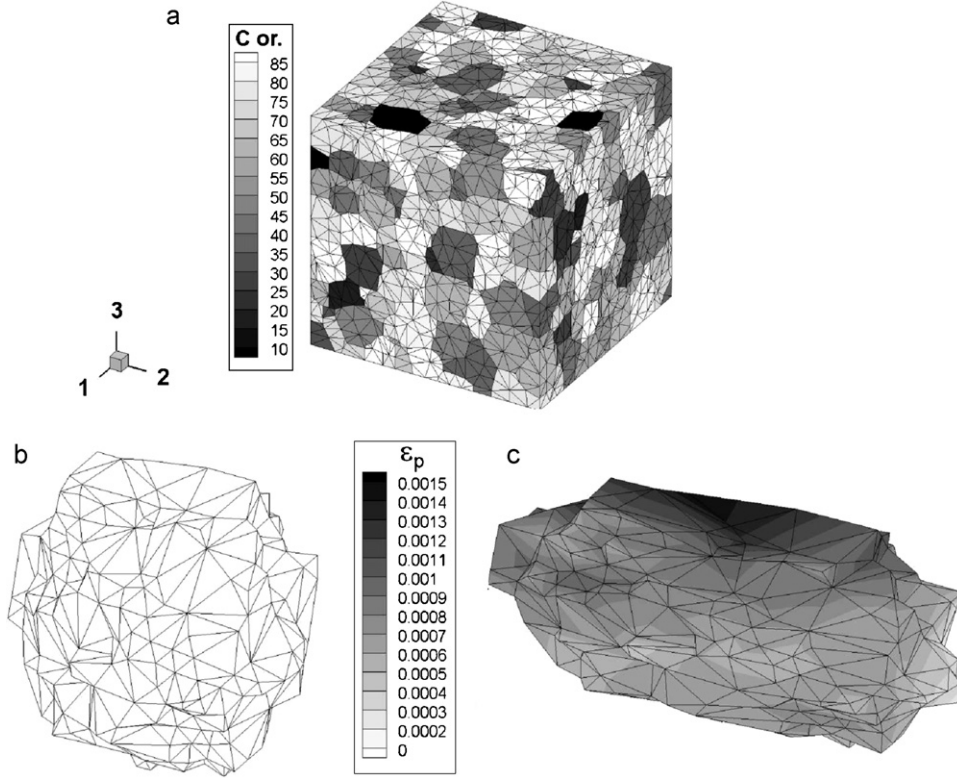


Fig. 6. Error plots in convergence study: (a) error of mean  $E_{av}$  and (b) standard deviation  $E_{sd}$ , of grain/colony size vs. number of grains ( $i$ ) in the simulated microstructure.

calculated from the data taken from the EBSD scan, which in this case is 5.22  $\mu\text{m}$ . Convergence plots for the synthetic microstructure generation algorithm in Fig. 6 show convergence in the grain/colony size statistics of average and standard deviation. Virtual microstructures consisting of less than 300 grains do not match the statistics very well. Microstructures of 1000 grains or above show only slight improvement. Since larger microstructures are computationally intensive with crystal plasticity FEM, microstructures containing 500–600 grains are chosen in this work.

### 2.3. Mesh generation

The 3D microstructure model generated by the above algorithm is a voxelized volume with individual grains having a phase identification and an orientation defined by 3 Euler angles as shown in Fig. 7. For crystal plasticity FEM analysis, the voxelized volume should be meshed with smooth grain boundaries. A pure voxel-based mesh causes a “stair-stepped” boundary between grains, which has been shown to be the source of local instabilities during simulations in [32]. The current work uses the 4-noded tetrahedral or TET4 elements to mesh the polycrystalline domain. This element uses linear interpolation functions for the displacements, resulting in constant element strains. In this work, converged meshes with respect to local stress and strain values in creep and constant strain rate simulations, are generated for the 500–600-grain microstructures. There is little sensitivity of response functions to further mesh refinement. The commercial mesh generator Simmetrix [33], is used to generate the finite element mesh shown in Fig. 7. First, a triangular surface mesh is generated along the interior grain boundaries and cube boundaries. Then, this triangular surface element mesh is extended into the full 3D volumetric tetrahedral mesh. The discretization yields approximately 100,000–120,000 elements



**Fig. 7.** Virtual microstructures before and after simulation: (a) the 500-grain polycrystalline microstructure after meshing, with grayscale contour plot showing *c*-axis orientation, (b) a single internal grain mesh before creep loading and (c) after 10,000 s of creep loading at 700 MPa (approx. 83% of YS) with grayscale contour plot showing plastic strain  $\epsilon_p$ . Deformation is scaled by a factor of 50. The *c*-axis orientation is defined as the angle between the loading direction (in this case the 2-direction) and the *c*-axis of the hcp phase of each grain/colony (the cube length dimension,  $l_0$ , is 68  $\mu\text{m}$ ).

and 20,000–22,000 nodes for the polycrystalline microstructure model.

The meshes are checked for distorted elements. It is observed that a very small number of elements (on the order of 0.01%) in the ensemble have aspect ratio of 40 or higher. Two different microstructures were generated that are statistically equivalent; one with 500 grains and one with 600 grains. Increasing the number of grains in the simulated microstructures above 500 grains however shows no effect on the simulated micromechanical creep response parameters as discussed in Section 3.

#### 2.4. Crystal plasticity finite element analysis of simulated polycrystalline microstructures

An isothermal, size-dependent and rate-dependent crystal plasticity finite-element computational model described and developed in [14–16] is used in conjunction with MSC/Marc Mentat and an in-house parallelized code to simulate the response of the synthetically generated microstructures of  $\alpha$ - $\beta$  Ti–6Al–4V under various loading and boundary conditions.

#### 2.5. Summary of the constitutive model

Deformation of crystalline materials is modeled by a combination of elastic stretching and rotation of crystal lattices, and plastic slip on different slip systems [10,34]. The stress–strain relation is expressed in terms of the second Piola–Kirchhoff stress  $\mathbf{S}$  ( $= \det \mathbf{F}^e \mathbf{F}^{e-1} \bar{\sigma} \mathbf{F}^{e-T}$ ) and the work conjugate Lagrange Green strain tensor  $\mathbf{E}^e$  ( $= (1/2)\{\mathbf{F}^{eT} \mathbf{F}^e - \mathbf{I}\}$ ) as,

$$\mathbf{S} = \mathbf{C} : \mathbf{E}^e, \quad (4)$$

where  $\mathbf{C}$  is the fourth-order anisotropic elasticity tensor,  $\bar{\sigma}$  is the Cauchy stress tensor, and  $\mathbf{F}^e$  is the elastic part of the deformation gradient defined by the relation,

$$\mathbf{F}^e \equiv \mathbf{F} \mathbf{F}^p^{-1}, \quad \det \mathbf{F}^e > 0. \quad (5)$$

where  $\mathbf{F}$  represents the deformation gradient and  $\mathbf{F}^p$  its plastic component. The incompressibility constraint is given by the condition  $\det \mathbf{F}^p = 1$ . The flow rule describing the plastic deformation is cast in terms of the plastic velocity gradient,

$$L^p = \dot{\mathbf{F}}^p \dot{\mathbf{F}}^{p-1} = \sum_{\alpha} \dot{\gamma}^{\alpha} \mathbf{s}_0^{\alpha} \quad (6)$$

with  $\dot{\gamma}^{\alpha} = \dot{\gamma} \left| \frac{\tau^{\alpha}}{g^{\alpha}} \right|^{1/m} \text{sign}(\tau^{\alpha})$ ,

where  $\dot{\gamma}^{\alpha}$  is the plastic shearing rate,  $\tau^{\alpha}$  is the resolved shear stress,  $g^{\alpha}$  is the slip system deformation resistance on the  $\alpha$ th slip system of a given phase.  $m$  is a material rate sensitivity parameter and the Schmid tensor,  $\mathbf{s}_0^{\alpha}$ , is expressed as

$$\mathbf{s}_0^{\alpha} \equiv \mathbf{m}_0^{\alpha} \otimes \mathbf{n}_0^{\alpha}. \quad (7)$$

The slip system deformation resistance  $g^{\alpha}$  evolves along with the hardening rates as described in [34,35] as

$$\dot{g}^{\alpha} = \sum_{\beta=1}^{n_{\text{slip}}} h^{\alpha\beta} \left| \dot{\gamma}^{\beta} \right| = \sum_{\beta} q^{\alpha\beta} h^{\beta} \left| \dot{\gamma}^{\beta} \right|, \quad (8)$$

where  $h^{\alpha\beta}$  is the strain hardening rate due to both self and latent hardening,  $h^{\beta}$  is the self-hardening rate and  $q^{\alpha\beta}$  is a matrix describing the latent hardening. For the hcp  $\alpha$ -phase, it is assumed that the

evolution of the self-hardening rate is governed by the following laws:

$$h^\beta = h_0^\beta \left| 1 - \frac{g^\beta}{g_s^\beta} \right|^r \text{sign} \left( 1 - \frac{g^\beta}{g_s^\beta} \right), \quad (9)$$

$$g_s^\beta = \tilde{g} \left( \frac{\dot{\gamma}^\beta}{\dot{\gamma}} \right), \quad (10)$$

where  $h_0^\beta$  is the initial hardening rate,  $g_s^\beta$  is the saturation slip deformation resistance, and  $r$ ,  $\tilde{g}$  and  $n$  are slip system hardening parameters. A different relation is used for the evolution for the bcc  $\beta$  phase within the transformed  $\beta$  colonies, as:

$$h^\beta = h_s^\beta + \text{sech}^2 \left[ \left( \frac{h_0^\beta - h_s^\beta}{\tau_s^\beta - \tau_0^\beta} \right) \gamma^\alpha \right] (h_0^\beta - h_s^\beta) \quad (11)$$

$$\gamma^\alpha = \int_0^t \sum_{\beta=1}^{n\text{slip}} |\dot{\gamma}^\beta| dt \quad (12)$$

Here  $h_0^\beta$  and  $h_s^\beta$  are the initial and asymptotic hardening rates,  $\tau_s^\beta$  represent the saturation value of the shear stress when  $h_s^\beta = 0$ , and  $\gamma^\alpha$  is a measure of total plastic shear.

A Hall–Petch-type equation has been introduced into the crystal plasticity relations in [16,17] to account for grain and lath size dependence of initial slip resistance, ensuing from the resistance to dislocation motion. This equation relates the initial slip system deformation resistance,  $g^\alpha$ , to a characteristic size as:

$$g^\alpha = g_0^\alpha + \frac{K^\alpha}{\sqrt{D^\alpha}} \quad (13)$$

where  $g_0^\alpha$  and  $K^\alpha$  are slip system parameters that refer to the interior slip system deformation resistance and slope, respectively, and  $D^\alpha$  is a characteristic length scale for each slip system governing the size effect. The  $D^\alpha$  values represent the initial mean-free path of dislocations, while hardening due to the creation of forest dislocations is captured by the evolution of  $g^\alpha$ . As described in [16], the  $D^\alpha$  values in the transformed  $\beta$  regions correspond to either the colony size, the  $\alpha$  lath thickness, or  $\beta$  rib thickness. The choice depends on the mean-free path of dislocation or the ease of slip within the colony lath structure. Consequently  $D^\alpha$  can be different for different slip systems. For the primary  $\alpha$  phase, the  $D^\alpha$  values are assumed to be the ESD of the grain for all slip systems, implying that the mean-free path is impeded by the grain boundaries.

### 2.6. Material properties

Elasticity and crystal plasticity parameters are calibrated from experimental results using a multi-variable optimization method developed in [36,15]. In [36,15] single crystals of  $\alpha$  Ti–6Al and single colonies of  $\alpha$ – $\beta$  Ti–6242 have been subjected to constant strain rate tests at different rates and creep tests. While those parameters are generally retained for analyses in this work, they have been re-examined for the material considered and minor changes are made where needed. Tables 2 and 3 give the components of the

**Table 2**  
Calibrated stiffness components of the transversely isotropic elasticity tensor for the hcp-phase.

$C_{ij}$ parameter	Value (GPa)
$C_{11}=C_{22}$	170.0
$C_{33}$	204.0
$C_{12}=C_{21}$	98.0
$C_{13}=C_{31}=C_{23}=C_{32}$	86.0
$C_{44}$	$C_{11}-C_{12}$
$C_{55}=C_{66}$	102.0
Other $C_{ij}$	0

**Table 3**  
Calibrated stiffness components of the cubic symmetric elasticity tensor for bcc-phase.

$C_{ij}$ parameter	Value (GPa)
$C_{11}=C_{22}=C_{33}$	250.21
$C_{13}=C_{31}=C_{23}=C_{32}=C_{12}=C_{21}$	19.0
$C_{44}=C_{55}=C_{66}$	230.65
Other $C_{ij}$	0

anisotropic elastic stiffness matrix for both the hcp and bcc phases. Tables 4–6 give the calibrated values of the crystal plasticity parameters for both the hcp and bcc phases in the transformed  $\beta$  colonies as well as the hcp parameters for the primary  $\alpha$  grains.

### 2.7. Boundary and loading conditions

Constant strain rate and creep simulations of the polycrystalline model are conducted in this work. To suppress rigid body modes, symmetric constraint conditions are applied, in which nodes on the back faces of the cube (see Fig. 7a) are constrained as  $u_1=0$  on the 1-face,  $u_2=0$  on the 2-face, and  $u_3=0$  on the 3-face. For constant strain rate simulations, one of the outer faces is imposed a constant strain rate displacement boundary condition of  $u_{ii}(t) = l_0(\exp(\dot{\epsilon}_{ii}^c t) - 1)$ . Here  $l_0$  is the initial dimension of the cube and  $\dot{\epsilon}_{ii}^c$  is the applied constant strain rate with  $i$  corresponding to the direction that the cube is loaded. For creep simulations, a constant load is applied to one of the outer faces. All other faces are traction free. An implicit backward Euler time-integration scheme is used for the solution to the time-dependent problem using the commercial finite element code MSC/Marc Mentat [37] using the user-defined material routine.

## 3. Comparison of the CPFEM model with experimental results

The CPFEM model results are compared with limited material properties of Ti–6Al–4V obtained from experimental data available from the supplier [38]. The material property available is the engineering yield strength  $YS=821$  MPa, defined by the 0.2% strain offset method for a tensile experiment conducted at a strain rate of  $10^{-4} \text{ s}^{-1}$ . The engineering stress–strain curve determined from the CPFEM simulation is shown in Fig. 8. The simulated yield strength is determined to be 833 MPa which reflects a 1.5% deviation from the experimental value of 821 MPa. The only change in the parameter

**Table 4**  
Calibrated parameters for the bcc slip systems in the homogenized transformed  $\beta$  colonies.

Parameters for slip system	$m$	$g_0^\alpha$ (MPa)	$\dot{\gamma}^\alpha$ ( $\text{s}^{-1}$ )	$h_0$	$h_s$	$\tau_0$ (MPa)	$\tau_s$ (MPa)	$K^\alpha$ (MPa $\sqrt{\mu\text{m}}$ )
{1 0 1}	0.02	450.00	0.0023	1500.0	25.0	500.0	200.0	413.4
{1 1 2} soft	0.02	429.82	0.0023	1371.6	25.0	500.0	200.0	413.4
{1 1 2} hard	0.02	409.63	0.0023	1979.8	25.0	500.0	200.0	315.9
{1 2 3} soft	0.02	451.28	0.0023	2312.0	25.0	500.0	200.0	413.4
{1 2 3} hard	0.02	400.67	0.0023	1634.8	25.0	500.0	200.0	315.9

**Table 5**  
Calibrated parameters for the hcp basal slip systems in the homogenized transformed  $\beta$  colonies.

Parameters for slip system	$m$	$g_0^\alpha$ (MPa)	$\dot{\gamma}$ ( $s^{-1}$ )	$h_0$	$r$	$\tilde{\gamma}$ (MPa)	$n$	$K^\alpha$ (MPa $\sqrt{\mu\text{m}}$ )
Basal $a_1$	0.02	284.0	0.0023	1500.0	0.30	450.0	0.14	147.4
Basal $a_2$	0.02	315.0	0.0023	2300.0	0.30	634.0	0.10	98.0
Basal $a_3$	0.02	243.0	0.0023	8000.0	0.40	371.0	0.05	98.0
Prismatic $a_1$	0.02	240.0	0.0023	3450.0	0.29	504.0	0.15	147.4
Prismatic $a_2$	0.02	210.0	0.0023	6500.0	0.20	583.0	0.25	15.8
Prismatic $a_3$	0.02	240.0	0.0023	3600.0	0.30	504.0	0.15	47.4
Pyr. (a)	0.02	395.0	0.0023	100.0	0.10	550.0	0.01	147.4
Pyr. (c+a)	0.02	623.3	0.0023	100.0	0.10	1650.0	0.01	147.4

**Table 6**  
Calibrated parameters for the slip systems in the primary  $\alpha$  grains.

Parameters for slip system	$m$	$g_0^\alpha$ (MPa)	$\dot{\gamma}$ ( $s^{-1}$ )	$h_0$	$r$	$\tilde{\gamma}$ (MPa)	$n$	$K^\alpha$ (MPa $\sqrt{\mu\text{m}}$ )
Basal (a)	0.02	284.00	0.0023	100.0	0.1	450.0	0.01	164.5
Prism. (a)	0.02	282.24	0.0023	100.0	0.1	550.0	0.01	164.5
Pyr. (a)	0.02	395.00	0.0023	100.0	0.1	550.0	0.01	164.5
Pyr. (c+a)	0.02	623.30	0.0023	100.0	0.1	1650.0	0.01	164.5

values over those in [36,15] is a 10% reduction in  $g_0^\alpha$ . This is deemed reasonable because parameters were not originally calibrated for this particular alloy. The agreement in the overall YS is encouraging. Fig. 7(b) shows a single internal grain after 10,000 s of creep loading at 700 MPa, which is approximately 83% of YS. The deformation is scaled by a factor of 50 and the contour plot shows plastic strain  $\epsilon_p$ .

#### 4. Microstructure-dependent macroscopic models for yield strength, creep and constant strain rate behavior

Microstructure–property relationships have been developed for titanium alloys through the use of neural network models in [11,12,30,39,40]. However, the time and cost associated with building these neural network models can be quite significant. They rely on a huge database of experimental data that span a wide range of values to be effective. Additionally, these models are often incapable of accounting for the true physics in the microstructure that govern the various properties. Sensitivity studies are performed in the present work to propose functional forms that relate microstructural features to mechanical properties. Only morphological parameters of the microstructure are considered in this study (crystallographic features are not considered).

##### 4.1. Constitutive model response parameters

The CPFEM results can be used effectively to derive macroscopic constitutive models of plastic deformation and creep in polycrystalline metals. In this study, two types of macroscopic models are considered. The Ramberg–Osgood equation [41] depicts the

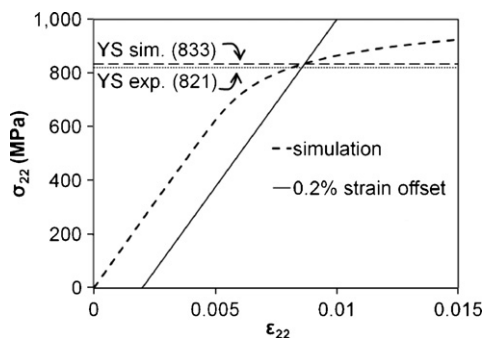


**Fig. 8.** Engineering stress–strain response with a comparison of the simulated and experimental YS. The 2-direction corresponds to the loading direction.

elastic–plastic constitutive relation in metallic materials at constant strain rates. It is expressed as:

$$\epsilon = \frac{\sigma}{E} + K \left( \frac{\sigma}{E} \right)^n, \quad (14)$$

where the first term represents the elastic portion of the strain,  $\epsilon_e$  and the second term represents the plastic portion of the strain,  $\epsilon_p$ .  $K$  and  $n$  are two dimensionless material parameters which are obtained from the CPFEM results. For describing the creep response, a power creep law proposed in Lubahn and Felgar is used [42] where the plastic strain component is expressed as a power law in time as:

$$\epsilon_p = At^m, \quad (15)$$

where  $t$  is time, and  $A$  (with units of  $s^{-1}$ ) and  $m$  (dimensionless) are material constants that are calibrated from creep simulation results in CPFEM. These constitutive relations manifest small strain response in the material and this behavior is explored in this study.

##### 4.2. Sensitivity analyses

An array of synthetic specimens is generated by varying the baseline microstructure discussed in Section 2.2 and simulated to conduct sensitivity analyses of response to changes in microstructural parameters. The reference microstructure is one generated by the synthetic microstructure generation procedure, for which, the sensitivity of response to variations in  $\alpha$  lath size  $l_\alpha$ ,  $\beta$  rib size  $l_\beta$ , volume fraction of primary  $\alpha$  grains  $V_f$ , and average grain/colony size  $D$  are studied. Each individual characteristic feature is varied while others are held constant in the sensitivity analysis. The response functions analyzed include yield strength, the Ramberg–Osgood parameters  $K$  and  $n$  in Eq. (14), and the power creep law parameters  $A$  and  $m$  in Eq. (15). The results of the sensitivity analyses of these microstructural features are shown in Figs. 9–28. The YS response is shown in Figs. 9–12, the power creep law parameters,  $A$  in Figs. 13–16 and  $m$  in Figs. 17–20, and the Ramberg–Osgood parameters,  $K$  in Figs. 21–24 and  $n$  in Figs. 25–28. The ranges of variation of the  $\alpha$  lath thicknesses and the corresponding  $\beta$  rib thicknesses are approximately 0.2–1.0  $\mu\text{m}$  and 0.1–0.3  $\mu\text{m}$ , respectively. These are realistic ranges observed in experiments, for which ranges that cover sizes differing by 500% are attained by varying processing cooling rates [13].

The simulation results show that in general changes to  $\alpha$  lath thickness and  $\beta$  rib thickness have a smaller effect on response compared to the larger effects seen from changes in volume fraction of primary  $\alpha$  grains and average grain/colony size. Figs. 9 and 10,

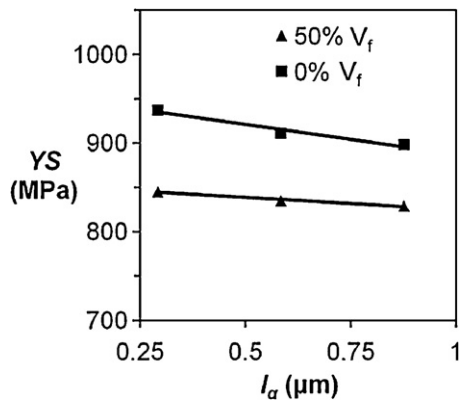


Fig. 9. Sensitivity of yield strength (YS) to  $\alpha$  lath thickness ( $l_\alpha$ ).

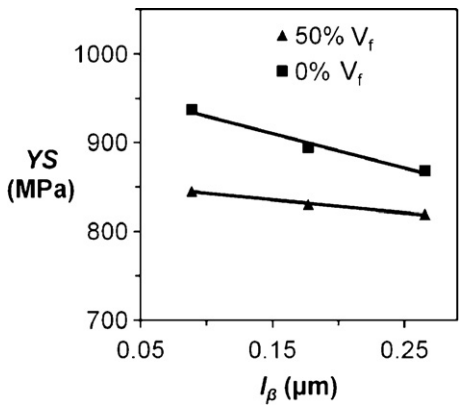


Fig. 10. Sensitivity of yield strength (YS) to  $\beta$  rib thickness ( $l_\beta$ ).

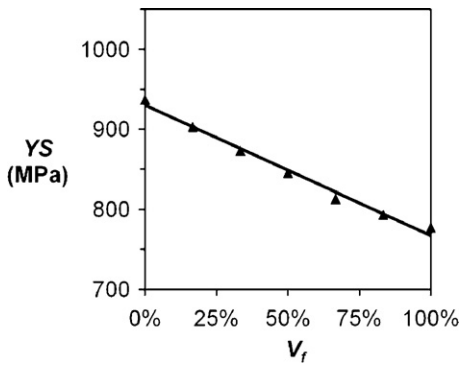


Fig. 11. Sensitivity of yield strength (YS) to volume fraction of primary  $\alpha$  ( $V_f$ ).

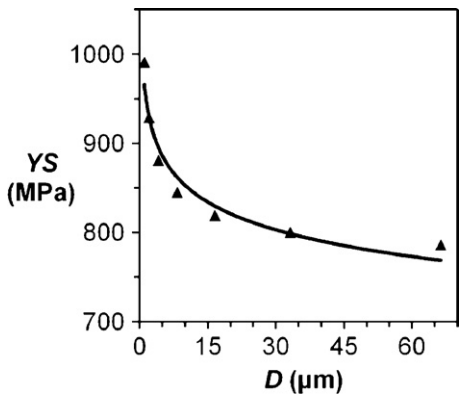


Fig. 12. Sensitivity of yield strength (YS) to average grain/colony size ( $D$ ).

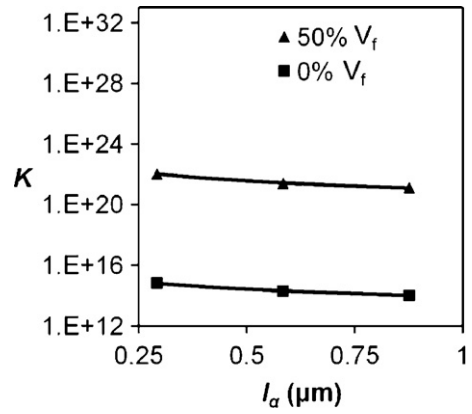


Fig. 13. Sensitivity of K parameter to  $\alpha$  lath thickness ( $l_\alpha$ ).

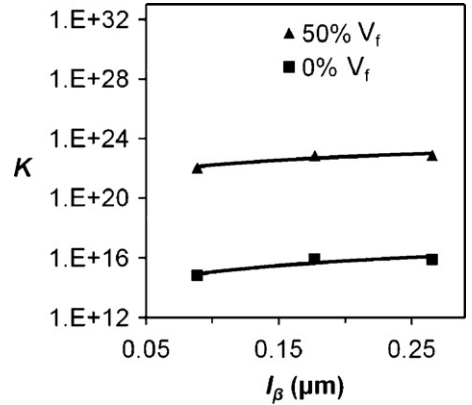


Fig. 14. Sensitivity of K parameter to  $\beta$  rib thickness ( $l_\beta$ ).

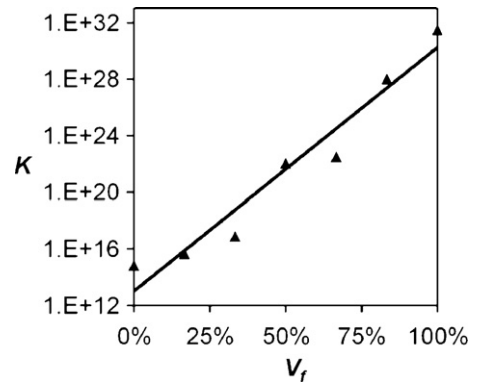


Fig. 15. Sensitivity of K parameter to volume fraction primary  $\alpha$  ( $V_f$ ).

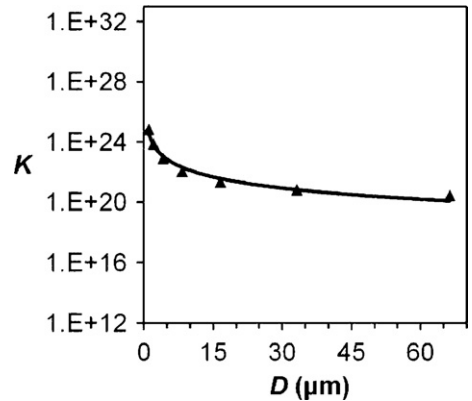


Fig. 16. Sensitivity of K parameter to grain/colony size ( $D$ ).

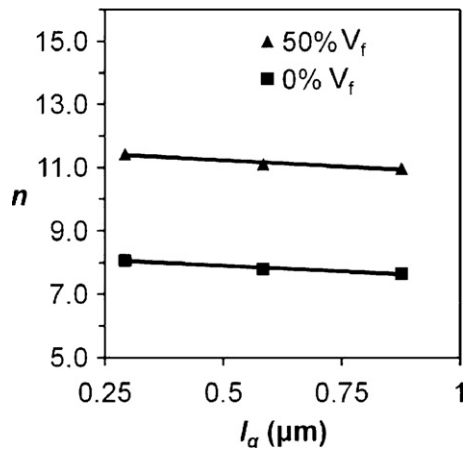


Fig. 17. Sensitivity of  $n$  parameter to  $\alpha$  lath thickness ( $l_\alpha$ ).

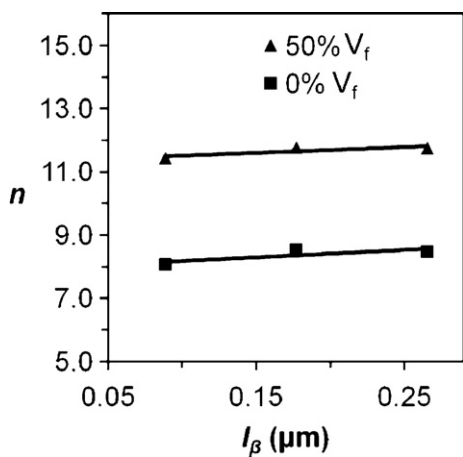


Fig. 18. Sensitivity of  $n$  parameter to  $\beta$  rib thickness ( $l_\beta$ ).

as well as the other figures which investigate the sensitivities of  $l_\alpha$  and  $l_\beta$ , also indicate the results for 0%  $V_f$  (corresponding to a 100% transformed  $\beta$  colony specimen). As would be expected, there is a greater sensitivity to changes in  $l_\alpha$  and  $l_\beta$  for the 0%  $V_f$  cases compared to the 50%  $V_f$  cases. This is explained by the fact that the primary  $\alpha$  grains have no lath or rib structure. The fewer of these pure  $\alpha$  grains in the structure, the higher the effect of changes to the  $\alpha$  lath and  $\beta$  rib thicknesses. Focusing on the sensitivity of YS to the various microstructural features in Figs. 9–12, the trend is consistent for

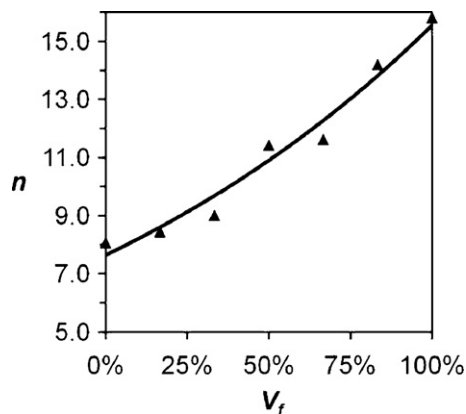


Fig. 19. Sensitivity of  $n$  parameter to volume fraction primary  $\alpha$  ( $V_f$ ).

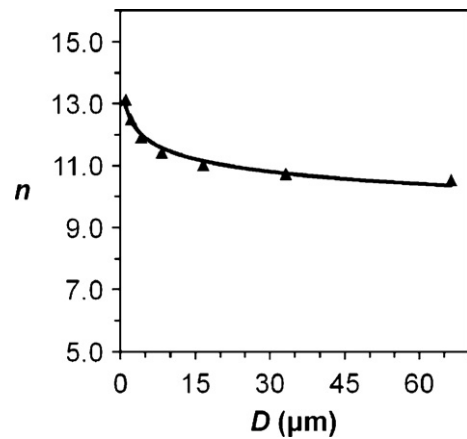


Fig. 20. Sensitivity of  $n$  parameter to grain/colony size ( $D$ ).

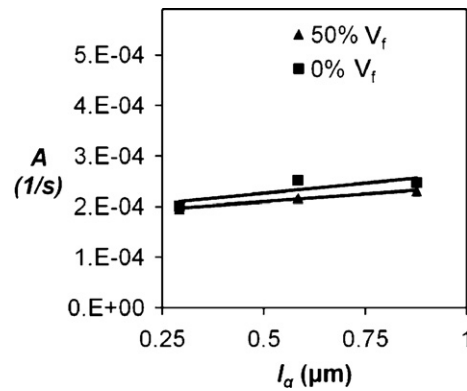


Fig. 21. Sensitivity of  $A$  parameter to  $\alpha$  lath thickness ( $l_\alpha$ ).

all features that as more grain/colony boundary or more lath/rib boundary is introduced into the microstructure the YS increases. This trend is in agreement with the understanding that boundaries impede dislocation motion and therefore hinder the onset of plastic deformation and ultimately increase the strength of a material.

It is worth noting the sensitivity of YS to the average grain/colony size in Fig. 12. This non-linear response shows a Hall-Petch-type dependence where with smaller grain sizes there is a very large sensitivity to changes in the grain size. As the grain sizes increase there is a saturation and not as much sensitivity to the grain size after the average grain size reaches around 20  $\mu\text{m}$ . These results are comparable with the experimental results in [43], where grain sizes as small as 1  $\mu\text{m}$  in  $\alpha$ - $\beta$  Ti have been achieved using hydrogen treatments. They have observed that the yield strength of the material

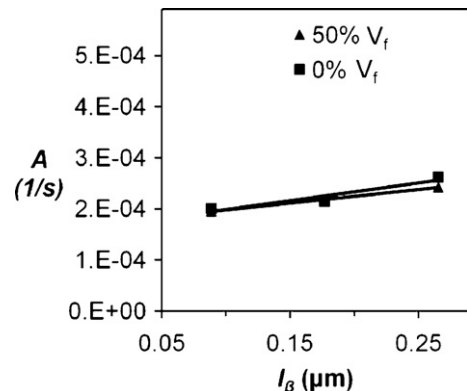


Fig. 22. Sensitivity of  $A$  parameter to  $\beta$  rib thickness ( $l_\beta$ ).

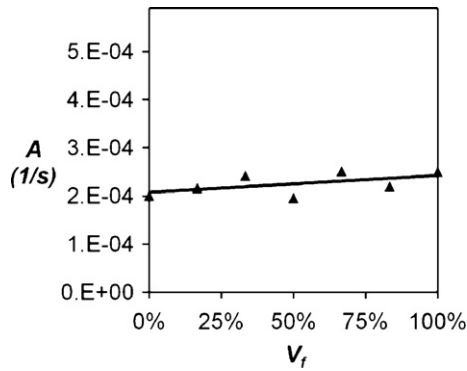


Fig. 23. Sensitivity of A parameter to volume fraction primary  $\alpha$  ( $V_f$ ).

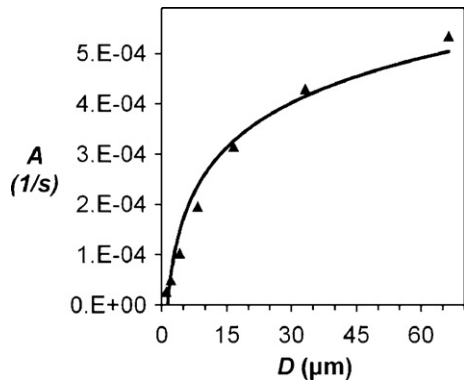


Fig. 24. Sensitivity of A parameter to grain/colony size ( $D$ ).

follows the Hall–Petch relationship at these values. Correspondingly, a two-parameter macroscopic yield strength relationship may be expressed as,

$$YS = \sigma_0 + \frac{K^*}{\sqrt{D}} \quad (16)$$

where  $\sigma_0$  and  $K^*$  are macroscopic size-effect constants.

Plotting YS as a function of  $1/D^{0.5}$  in Fig. 29, yields a value of  $\sigma_0 = 760$  MPa and  $K^* = 240$  MPa $\sqrt{\mu\text{m}}$ , from a straight line fit. These values are comparable to those obtained in [16] for a specimen of Ti-6242, viz. 750 MPa and 250 MPa $\sqrt{\mu\text{m}}$ , respectively. The simulated macroscopic response with Hall–Petch effect is expected due to explicit Hall–Petch effects in the grain scale model in Eq. (13). Comparing the grain scale parameters in Tables 4–6 with the macroscopic values determined above, it is seen that the average  $K^*$

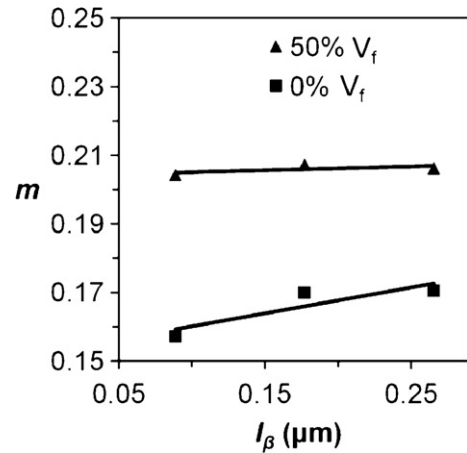


Fig. 26. Sensitivity of  $m$  parameter to  $\beta$  rib thickness ( $l_\beta$ ).

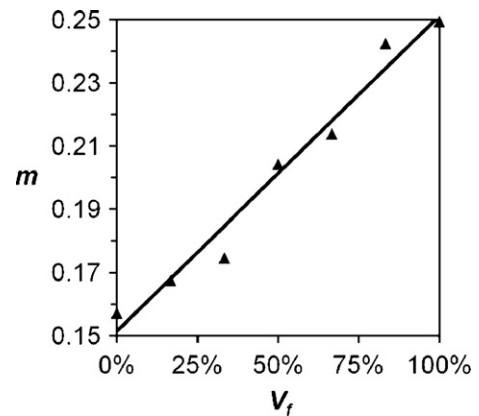


Fig. 27. Sensitivity of  $m$  parameter to volume fraction primary  $\alpha$  ( $V_f$ ).

value of approximately 200 MPa $\sqrt{\mu\text{m}}$  is close to the macroscopic  $K^*$  value. When the average  $g_0^\alpha$  grain scale value (approximately 370 MPa) is compared with the macroscopic value of  $\sigma_0 = 760$  MPa, it is seen that the macroscopic value is around two times its magnitude. This result is a direct consequence of the difference between the macroscopic model's  $D$  dependence and the grain scale model's  $D^\alpha$  dependence. Recall that the transformed  $\beta$  regions have  $D^\alpha$  values, which correspond either to the colony size, the  $\alpha$  lath thickness, or  $\beta$  rib thickness depending on ease of slip conditions at the hcp–bcc interfaces of the colony lath structure. Because the

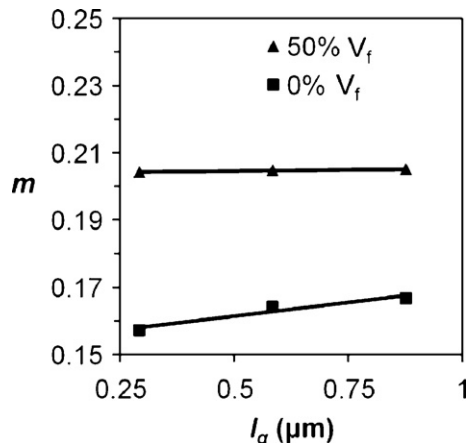


Fig. 25. Sensitivity of  $m$  parameter to  $\alpha$  lath thickness ( $l_\alpha$ ).

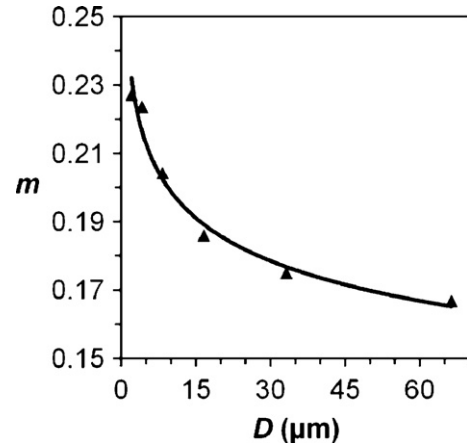


Fig. 28. Sensitivity of  $m$  parameter to grain/colony size ( $D$ ).

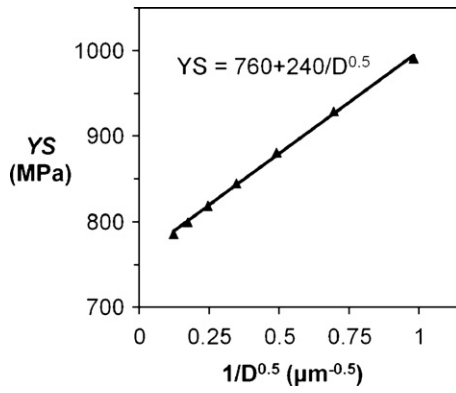


Fig. 29. Hall-Petch two parameter model.

material is comprised of around 50% transformed  $\beta$  colonies, the average characteristic length scale  $D^\alpha$  of all the grains/colonies in the sample is driven below the average grain/colony size  $D$  of  $11.9 \mu\text{m}$ . Very simply, the lath/rib structure in the material tends to drive the average  $D^\alpha$  down which drives the macroscopic  $\sigma_0$  value higher. For titanium alloys comprised of 100% primary  $\alpha$  it is expected that  $\sigma_0$  would be in the same range as the average  $g_0^\alpha$ .

Focusing attention to Figs. 12, 16, 20, 24 and 28, the effect of average grain size  $D$  on all the response parameters can be compared. As for YS, parameters  $K$ ,  $n$ ,  $A$  and  $m$  show the similar characteristic of high sensitivity at low grain sizes and a lessened sensitivity as grain size increases.

#### 4.3. Functional forms

From the sensitivity studies, functional forms that connect critical microstructural features with each material response parameter for the stress-strain and creep relations in Eqs. (14) and (15) are developed. The forms are developed with the assumption that the effects of the microstructural variables are uncorrelated. The yield strength, YS (MPa), as a function of  $\alpha$  lath thickness,  $l_\alpha$  ( $\mu\text{m}$ ),  $\beta$  rib thickness,  $l_\beta$  ( $\mu\text{m}$ ), volume fraction of primary  $\alpha$ ,  $V_f$ , and average grain/colony size,  $D$  ( $\mu\text{m}$ ), is determined to be:

$$YS(l_\alpha, l_\beta, V_f, D) = k_{YS} \times YS(l_\alpha) \times YS(l_\beta) \times YS(V_f) \times YS(D) \quad (17)$$

where

$$YS(l_\alpha) = -27.4l_\alpha + 852$$

$$YS(l_\beta) = -147l_\beta + 857$$

$$YS(V_f) = -163V_f + 930$$

$$YS(D) = 760 + \frac{240}{\sqrt{D}}$$

$$k_{YS} = 1.62 \times 10^{-9}$$

The influence of the average size  $D$  is found to be the smallest in comparison with the other characteristics. The functional form connecting  $l_\alpha$  to YS, is compared with results of a linear regression model based on neural network modeling in [11]. The neural network modeling in [11] uses experimental yield strength results from approximately 75 different Ti-6Al-4V samples, heat treated to produce different  $\alpha$  lath thicknesses. Results of the comparison are shown in Fig. 30. While the slopes deviate a little, the agreement is deemed satisfactory, given the completely different circumstances under which these two models are constructed.

The Ramberg-Osgood parameter  $K$  (unitless), as a function of  $\alpha$  lath thickness  $l_\alpha$  ( $\mu\text{m}$ ),  $\beta$  rib thickness  $l_\beta$  ( $\mu\text{m}$ ), volume fraction of

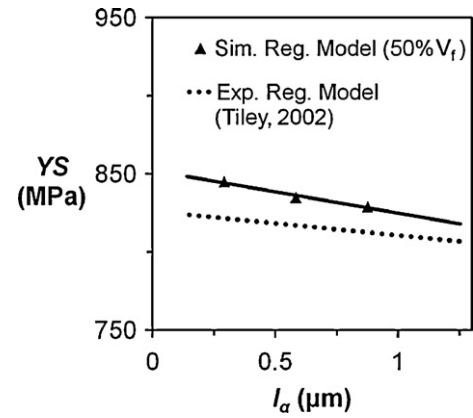


Fig. 30. Comparison of YS vs.  $l_\alpha$  developed using (i) the functional form in Eq. (17) and (ii) the linear regression model obtained from neural network modeling of experimental data in [11].

primary  $\alpha$   $V_f$ , and average grain/colony size  $D$  ( $\mu\text{m}$ ), is determined to be:

$$K(l_\alpha, l_\beta, V_f, D) = k_K \times K(l_\alpha) \times K(l_\beta) \times K(V_f) \times K(D) \quad (18)$$

where

$$K(l_\alpha) = 9.44 \times 10^{20} l_\alpha^{-1.97}$$

$$K(l_\beta) = 1.21 \times 10^{24} l_\beta^{1.88}$$

$$K(V_f) = 1.03 \times 10^{13} e^{39.7V_f}$$

$$K(D) = 3.89 \times 10^{24} D^{-2.48}$$

$$k_K = 9.22 \times 10^{-67}$$

The effect of the volume fraction is found to be dominant over other characteristics for the functional dependence of  $K$ . The functional form of the Ramberg-Osgood parameter  $n$  (unitless) as a function of  $l_\alpha$  ( $\mu\text{m}$ ),  $l_\beta$  ( $\mu\text{m}$ ),  $V_f$ , and  $D$  ( $\mu\text{m}$ ) is determined to be:

$$n(l_\alpha, l_\beta, V_f, D) = k_n \times n(l_\alpha) \times n(l_\beta) \times n(V_f) \times n(D) \quad (19)$$

where

$$n(l_\alpha) = -0.794l_\alpha + 11.6$$

$$n(l_\beta) = 1.82l_\beta + 11.3$$

$$n(V_f) = 7.65e^{0.710V_f}$$

$$n(D) = 13.0D^{-0.00536}$$

$$k_n = 6.24 \times 10^{-4}$$

Here again, the volume fraction has a significant influence on  $n$  while the average size has very little effect on  $n$ . The creep parameter  $A$  ( $\text{s}^{-1}$ ) as a function of  $l_\alpha$  ( $\mu\text{m}$ ),  $l_\beta$  ( $\mu\text{m}$ ),  $V_f$ , and  $D$  ( $\mu\text{m}$ ) is determined to be:

$$A(l_\alpha, l_\beta, V_f, D) = k_A \times A(l_\alpha) \times A(l_\beta) \times A(V_f) \times A(D) \quad (20)$$

where

$$A(l_\alpha) = 5.95 \times 10^{-5} l_\alpha + 1.80 \times 10^{-4}$$

$$A(l_\beta) = 2.66 \times 10^{-4} l_\beta + 1.71 \times 10^{-4}$$

$$A(V_f) = 3.50 \times 10^{-5} V_f + 2.07 \times 10^{-4}$$

$$A(D) = 1.29 \times 10^{-4} \ln(D) - 3.57 \times 10^{-5}$$

$$k_A = 9.59 \times 10^{10}$$

For this parameter the  $\alpha$  and  $\beta$  thicknesses and volume fraction have linear effects, while the average size has a less logarithmic effect. Finally the creep parameter  $m$  (unitless) as a function of  $l_\alpha$  ( $\mu\text{m}$ ),  $l_\beta$  ( $\mu\text{m}$ ),  $V_f$ , and  $D$  ( $\mu\text{m}$ ) is expressed as:

$$m(l_\alpha, l_\beta, V_f, D) = k_m \times m(l_\alpha) \times m(l_\beta) \times m(V_f) \times m(D) \quad (21)$$

where

$$m(l_\alpha) = 0.00149l_\alpha + 0.204$$

$$m(l_\beta) = 0.0111l_\beta + 0.204$$

$$m(V_f) = 0.0998V_f + 0.151$$

$$m(D) = 0.249D^{-0.01}$$

$$k_m = 118.$$

## 5. Summary

This paper proposes a comprehensive computational procedure to meaningfully advance the state of the art in developing functional dependencies of material response functions on microstructural characteristics. The objectives proposed here are coherent with the recently proposed ICME or *Integrated Materials Engineering* paradigm of integrating materials in performance and process modeling [44]. The computational system comprises a relatively efficient data collection and processing procedure, a robust synthetic microstructure generating program, a mesh generation software, and a crystal plasticity based finite element analysis (CPFEM) program. This computational system is implemented to accurately predict the constant strain rate response and primary and secondary creep response of Ti–6Al–4V. Results of the computational system are compared with limited experimental data for validation. In addition, large sets of model microstructures with vastly different characteristics are generated and used to develop functional forms that relate microstructural characteristics to various response functions, viz. yield strength, creep parameters, and Ramberg–Osgood parameters. Sensitivity analyses are performed to determine functional forms of the response functions in terms of critical morphological parameters. Crystallographic parameters have not been considered in this study and will be the subject of a future study. The proposed functional form is compared with results of a neural network based model representing the dependence of the material yield strength on  $\alpha$  lath thickness. The functional forms depicting dependencies in microstructure–property relations are expected to provide guidance on effective material design.

## Acknowledgements

This work has been sponsored in part by the US National Science Foundation (Grant # CMMI-0800587, Program Manager: Dr. Clark Cooper) and the ONR/DARPA D3D Project (Grant # N00014-05-1-0504, Program Manager: Dr. Julie Christodoulou). Computer support by the Ohio Supercomputer Center through grant # PAS813-2 is also acknowledged. The authors are grateful to Prof. Hamish Fraser and Brian Welk for help with characterization.

## References

- [1] G. Lutjering, J. Williams, Titanium, Springer, 2003.
- [2] S. Suri, T. Neeraj, G.S. Daehn, D.H. Hou, J.M. Scott, R.W. Hayes, M.J. Mills, Mater. Sci. Eng. A 236 (1997) 996–999.
- [3] S. Suri, G.B. Viswanathan, T. Neeraj, D.H. Hou, M. Mills, Acta Metall. 47 (3) (1999) 1019–1034.
- [4] T. Neeraj, D.-H. Hou, G.S. Daehn, M.J. Mills, Acta Mater. 48 (2000) 1225–1238.
- [5] S. Karthikeyan, G.B. Viswanathan, P.I. Gouma, V.K. Vasudevan, Y.W. Kim, M.J. Mills, Mater. Sci. Eng. A 329–331 (2002) 621–630.
- [6] T. Neeraj, M.J. Mills, Mater. Sci. Eng. A 321 (2001) 415–419.
- [7] M.F. Savage, T. Neeraj, M.J. Mills, Metall. Mater. Trans. A 33 (2002) 891.
- [8] G. Viswanathan, S. Karthikeyan, R.W. Hayes, M.J. Mills, Acta Mater. 50 (20) (2002) 4965–4980.
- [9] R.W. Hayes, G.B. Viswanathan, M.J. Mills, Acta Mater. 50 (20) (2002) 4953–4963.
- [10] S. Balasubramanian, L. Anand, Acta Mater. 50 (2002) 133–148.
- [11] J. Tiley, Modeling of microstructure property relationships in Ti–6Al–4V, Ph.D. thesis, The Ohio State University, 201 West 19th Avenue, Columbus, OH 43210, 2002.
- [12] P. Collins, A combinatorial approach to the development of composition–microstructure–property relationships in titanium alloys using directed laser deposition, Ph.D. thesis, The Ohio State University, 201 West 19th Avenue, Columbus, OH 43210, 2004.
- [13] E. Lee, Microstructure evolution and microstructure: mechanical properties relationships in alpha–beta titanium alloys, Ph.D. thesis, The Ohio State University, 201 West 19th Avenue, Columbus, OH 43210, 2004.
- [14] V. Hasija, S. Ghosh, M.J. Mills, D. Joseph, Acta Mater. 51 (15) (2003) 4533–4549.
- [15] D. Deka, D. Joseph, S. Ghosh, M. Mills, Metall. Mater. Trans. A 37 (5) (2006) 1371–1388.
- [16] G. Venkatramani, S. Ghosh, M. Mills, Acta Mater. 55 (2007) 3971–3986.
- [17] G. Venkatramani, K. Kirane, S. Ghosh, Int. J. Plast. 28 (2008) 428–454.
- [18] K. Kirane, S. Ghosh, Int. J. Fatigue 30 (2008) 2127–2159.
- [19] M. Anahid, M. Samal, S. Ghosh, J. Mech. Phys. Solids 59 (2011) 2157–2176.
- [20] S. Ghosh, M. Anahid, P. Chakraborty, in: S. Ghosh, D. Dimiduk (Eds.), Computational Methods for Microstructure–Property Relations, Springer, 2010, pp. 497–554.
- [21] M. Groeber, Development of an automated characterization–representation framework for the modeling of polycrystalline materials in 3D, Ph.D. thesis, The Ohio State University, 201 West 19th Avenue, Columbus, OH 43210, 2007.
- [22] M.A. Groeber, B. Haley, M. Uchic, D. Dimiduk, S. Ghosh, Mater. Charact. 57 (2006) 259–273.
- [23] Y. Bhandari, S. Sarkar, M. Groeber, M. Uchic, D. Dimiduk, S. Ghosh, Comput. Mater. Sci. 42 (2007) 222–235.
- [24] M. Groeber, S. Ghosh, M. Uchic, D. Dimiduk, Acta Mater. 56 (2008) 1257–1273.
- [25] D.J. Rowenhorst, P.W. Voorhees, Metall. Mater. Trans. A 36 (2005) 2127–2135 (August).
- [26] E. Lauridsen, S. Schmidt, S. Nielsen, L. Margulies, H. Poulsen, D. Jensen, Scr. Mater. 55 (1) (2006) 51–56.
- [27] J.C. Russ, R.T. Dehoff, Practical Stereology, 2nd edition, Plenum Press, 1999.
- [28] V. Randle, G. Rohrer, Y. Hu, Scr. Mater. 58 (2008) 183–186.
- [29] T. Searles, Microstructural characterization of the  $\alpha/\beta$  titanium alloy Ti–6Al–4V, Master's thesis, The Ohio State University, 201 West 19th Avenue, Columbus, OH 43210, 2005.
- [30] S. Kar, Modeling of mechanical properties in alpha/beta-titanium, Ph.D. thesis, The Ohio State University, 201 West 19th Avenue, Columbus, OH 43210, 2005.
- [31] A. Edwards, Likelihood, Cambridge University Press, 1972.
- [32] T. Kanit, Int. J. Solids Struct. 40 (13–14) (2003) 3647–3679.
- [33] MeshSim User's Guide, Simmetrix Inc., Clifton Park, NY 12065, 2003.
- [34] M. Kothari, L. Anand, J. Mech. Phys. Solids 46 (1) (1998) 51–83.
- [35] S. Harren, T.C. Lowe, R.J. Asaro, A. Needleman, Philos. Trans. R. Soc. Lond. A: Math. Phys. Sci. 328 (1600) (1989) 443–500.
- [36] V. Hasija, S. Ghosh, M. Mills, D. Joseph, Acta Mater. 51 (2003) 4533–4549.
- [37] MSC Software Corporation, Santa Ana, CA, MSC Marc-Mentat (2009).
- [38] Titanium Metals Corporation, Toronto, OH, TIMET Co.
- [39] S. Kar, T. Searles, E. Lee, G. Viswanathan, J. Tiley, R. Banerjee, H. Fraser, Metall. Mater. Trans. A 37 (2006) 559–566.
- [40] B. Welk, Microstructural and property relationships in titanium alloy Ti–5553, Master's thesis, The Ohio State University, 201 West 19th Avenue, Columbus, OH 43210, 2010.
- [41] W. Ramberg, W. Osgood, National Advisory Committee For Aeronautics 902.
- [42] J. Lubahn, R. Felgar, Wiley Series on the Science and Technology of Materials: Plasticity, Creep, Metals.
- [43] H. Yoshimura, J. Alloys Compd. 293–295 (1–2) (1999) 858–861.
- [44] J. Allison, D. Backman, L. Christodoulou, J. Met. (November) (2006) 25–27.